Synaptic dysfunction caused by truncated tau is associated with hyperpolarization-activated cyclic nucleotide-gated channelopathy

Despoina Goniotaki[1], Francesco Tamagnini[2], Luca Biasetti[3], Svenja-Lotta Rumpf[1], Kate Fennell[3], Saskia J. Pollack[1], Shalom Ukwesa[1], Haoyue Sun[1], Louise C. Serpell[3], Wendy Noble[1], Kevin Staras[3], Diane P. Hanger[1, *]

[1]Department of Basic and Clinical Neuroscience,
Institute of Psychiatry, Psychology & Neuroscience, King's College London, UK
[2]School of Pharmacy, University of Reading, Reading, UK
[3]Sussex Neuroscience, School of Life Sciences, University of Sussex, UK
*Correspondence: diane.hanger@kcl.ac.uk

Neurodegenerative tauopathies are characterized by deposition in the brain of highly phosphorylated and truncated forms of tau, but how these impact on cellular processes remains unknown. Here, we show that hyperpolarization-induced membrane voltage 'sag', which is dependent on hyperpolarization-activated inward-rectifying (I_h) current and hyperpolarization-activated cyclic nucleotide-gated (HCN) cation channels, is increased in the Tau35 mouse model of human tauopathy. Expression of Tau35, corresponding to a fragment comprising the carboxy-terminal half of tau first identified in human tauopathy brain, reduces dendritic branching in mouse brain and in cultured hippocampal neurons, and decreases synaptic density. Neuronal expression of Tau35 results in increased tau phosphorylation and significant disruption to synaptic ultrastructure, including marked and progressive reductions in synaptic vesicle counts and vesicle cluster density. Ultrastructural analysis reveals that the positioning of synaptic vesicles is perturbed by Tau35, causing vesicles to accumulate at sites adjacent to the active zone and at the lateral edges of the cluster. These structural changes induced by Tau35 correlate with functional abnormalities in network activity, including increased width, reduced frequency and slower rate of rise of spontaneous excitatory postsynaptic currents. Collectively, these changes are consistent with a model in which disease-associated tau species disrupt network connectivity and signaling. Our results suggest that the persistence of truncated tau in the brain may underpin the catastrophic synaptic dysfunction observed during the development and progression of human tauopathy.

Keywords: tau, tauopathy, Tau35, dementia, HCN channels, sag, synapses, dendritic spines, synaptic vesicles

---

Introduction

Synapses are the principal structural and functional units that enable information signaling between neurons (Sudhof and Malenka, 2008). Although synaptic dysfunction is an early correlate of dementia, the pathophysiology of aberrant synaptic signaling remains poorly understood (Scheff *et al.*, 2006; Wishart *et al.*, 2006). One likely candidate to mediate damage to synapses is tau, a microtubule-associated protein that plays important roles in maintenance of the neuronal cytoskeleton, axonal transport,

synapse formation and synaptic integrity (Guo *et al.*, 2017). In healthy neurons, tau is primarily presynaptic, due to its high affinity for axonal microtubules (Hirokawa *et al.*, 1996). Tau also scaffolds and coordinates key signaling molecules at defined subcellular locations (Gotz *et al.*, 2013; Shaw and Filbert, 2009). Functional roles for tau at the synapse have previously been proposed (Hanger *et al.*, 2019; Hoover *et al.*, 2010; Pooler *et al.*, 2014; Tracy and Gan, 2018) and tau is involved in synaptic vesicle mobilization through its interaction with annexins (Gauthier-Kemper *et al.*, 2011; Stefanoska *et al.*, 2018) and vesicular proteins, including synapsin-I, α-synuclein, synaptogyrin-3, synaptotagmin (Liu *et al.*, 2016; McInnes *et al.*, 2018; Zhou *et al.*, 2017), and potassium ion channels (Hall *et al.*, 2015). In human tauopathies and in mouse models of disease, accumulation of phosphorylated tau, altered tau processing and aberrant tau localization, occur in parallel with reduced presynaptic protein expression, synapse density and synaptic function, suggesting a causal role for tau in disease pathogenesis (Bondulich *et al.*, 2016; Crespo-Biel *et al.*, 2012; Henstridge *et al.*, 2019; Jackson *et al.*, 2017; Kneynsberg *et al.*, 2017; Lleo *et al.*, 2019; Moreno *et al.*, 2016).

Voltage-gated hyperpolarization-activated cyclic nucleotide-gated (HCN) channels 1-4 are a family of non-selective cation channels (Wahl-Schott and Biel, 2009), that are emerging as potentially important targets in the pathogenesis of several neurodegenerative diseases, including tauopathies (Chang *et al.*, 2019; Musial *et al.*, 2018). HCN channels 1-4 are involved in multiple synaptic processes including regulation of membrane resistance, intrinsic membrane excitability, synaptic potential, and synaptic vesicle exocytosis (He *et al.*, 2014; Huang *et al.*, 2017; Shah, 2014). Notably, HCN channels selectively associate with regulatory proteins in dendritic spines, resulting in fine-tuning of network connectivity (Paspalas *et al.*, 2013). HCN channel activation generates an inward-rectifying (I_h) current, which reduces dendritic summation and affects synaptic vesicle release through interaction with calcium channels (Huang *et al.*, 2011; Magee, 1999; Tsay *et al.*, 2007). Notably, increased HCN channel expression dampens spontaneous synaptic vesicle release in adult entorhinal cortex (Huang *et al.*, 2011). Together with the synaptic changes observed in tauopathies, this indicates that HCN channels may be involved in the development and progression of neurodegenerative disease.

It has been previously established that Tau35 mice develop progressive tauopathy, including increased tau phosphorylation and deposition of abnormal tau species in the brain, in parallel with deficits in cognitive and motor functioning, and a reduced lifespan (Bondulich *et al.*, 2016). Here we show that Tau35 progressively modifies HCN channel properties in young and old animals, and in isolated neurons. We also demonstrate significant detrimental effects of fragmented tau on synaptic connectivity, ultrastructure and associated functional abnormalities in network activity. Our findings identify a new mechanism, mediated by HCN channels, that could explain the progressive synaptic dysfunction that underlies key aspects of human tauopathy.

Results

Increased tau phosphorylation and HCN channel expression in Tau35 mice

We first determined that tau phosphorylation is increased in the brains of Tau35 compared to wild-type (WT) mice at 4 months (pre-symptomatic) and 10 months, an age at which overt hippocampal tau pathology is apparent (Bondulich *et al.*, 2016). Using western blots of brain homogenates probed with antibodies to phosphorylated (PHF1 epitope, Ser396/Ser404) and total tau, increased phosphorylated tau was apparent in Tau35 mice at both ages, in the absence of any changes in total tau (Figure 1A, B). Examination of HCN1 and HCN3 channel expression in the brains of Tau35 mice (aged 4 and 10 months) revealed increased expression of both channels, which became significant for HCN1 at 10 months of age and for HCN3 at both ages (Figure 1C, D). We next determined that PHF1 labeling was also increased in Tau35 cultured hippocampal neurons (14 DIV), indicating that tau phosphorylation is elevated from an early stage of neuronal development in Tau35 mice (Figure 2A). Similarly, HCN1 and HCN3 channels were increased by 52% and 61%, respectively, in Tau35 hippocampal neurons (Figure 2B). Immunofluorescence labeling confirmed that both HCN1 and HCN3 are expressed in hippocampal neurons and that the fluorescence intensity was markedly increased by Tau35 (Figure 2C). HCN1 channel expression increased by 59% and HCN3 by 38%, in Tau35 neurons (Figure 2C). In contrast, there were no genotype-dependent changes in immunofluorescence of either HCN2 or HCN4 channels in Tau35 hippocampal neurons (Figure S1A). These data demonstrate striking elevations in tau phosphorylation and HCN1 and HCN3 channel expression in brain and in isolated hippocampal neurons from Tau35 mice. Our findings suggest a link between tauopathy and potentially altered network connectivity and dampened spontaneous hippocampal synaptic vesicle release induced by Tau35 expression in these mice.

Tau35 induces functional alterations in I_h-dependent sag in hippocampal neurons

To determine whether Tau35 affects neuronal excitability in early development, we performed whole-cell recordings in Tau35 and WT hippocampal neurons at 11-16 DIV. Upon injection of a hyperpolarizing current, plasma membrane voltage (V_m) deflection was suggestive of increased I_h-dependent sag in Tau35 neurons (Figure 3A). Notably, both HCN channel-dependent sag and rebound (Hu *et al.*, 2002) were significantly increased in Tau35 neurons. Sag_{sub} increased approximately two-fold and sag_{fit} was elevated almost 15-fold in Tau35 compared to WT hippocampal neurons (Figure 3B). The increased sag was paralleled by a three-fold rise in rebound potential when the hyperpolarizing current was interrupted in Tau35 neurons (Figure 3B). Since sag potentials increase in response to activation of I_h current through HCN channels (Richter *et al.*, 2000), our data indicate that this augmented sag is due to increased expression of HCN1 and HCN3 channels in Tau35 neurons (Figure 2C). In contrast, we detected no changes in the biophysical properties of non-inactivating potassium channels in Tau35 hippocampal neurons (Figure S2A). Specifically, Tau35 did not affect either the maximal conductance (Gmax) or the half-activation voltage ($V_{1/2}$) of isolated hippocampal neurons (Figure S2B). Taken together, our findings of selective increases in HCN channel conductance and expression in Tau35 neurons, are consistent with and provide a possible explanation for the increased I_h-dependent sag observed in other

models of tauopathy, such as rTg4510 transgenic mice that overexpress mutant P301L tau (Booth *et al.*, 2016b).

Reduced dendritic complexity in hippocampal neurons of Tau35 mice

We hypothesized that the observed alterations in synaptic function induced by Tau35 expression could disrupt network connectivity and signaling and thereby underlie key phenotypic aspects of tauopathy. To determine the consequences of Tau35 expression on neuronal structure, we quantified dendritic arborization as a correlate of synaptic strength (Peng *et al.*, 2009). Sholl analysis of Golgi-Cox stained brain sections of the CA1 region of mouse hippocampus (Figure 4A,B) revealed significant reductions in the number of dendritic branch points and mean dendrite lengths, but not in the soma area of Tau35 neurons compared to age-matched (10 months) WT control mice (Figure 4C). The Sholl analysis of all branches showed that expression of Tau35 significantly decreases overall dendritic arborization of hippocampal neurons (two-way ANOVA, $p < 0.0001$), which may be a correlate of diminished synaptic strength in Tau35 mice. In contrast, Sholl analysis of the CA1 region in Tau35 and WT mice aged 4 months, an age at which Tau35 mice exhibit minimal tau pathology, did not reveal any significant differences in the number of dendritic branch points, mean dendrite length, or soma area (Figure S3). Our results show that Tau35 expression causes a reduction in dendritic arborization in older animals. Furthermore, this loss of neuronal connectivity parallels the appearance of distinct tau pathology and cognitive decline in Tau35 mice (Bondulich *et al.*, 2016).

Reduced dendritic branching and spine density in primary Tau35 hippocampal neurons

We next examined the structure of primary hippocampal neurons cultured from Tau35 and WT mice. Sholl analysis was performed on neurons transfected with a plasmid expressing enhanced green fluorescent protein (eGFP) at 4 DIV and cultured until 6, 9, and 14 DIV. We observed no effect of Tau35 on dendritic branching, mean dendrite length, or soma area at 6 DIV (Figure S4A), and only a modest, but statistically significant reduction in branching by 9 DIV (Figure S4B, Two-way ANOVA ($p < 0.01$)). However, similar to our findings in the brains of Tau35 mice, hippocampal neurons cultured from these animals exhibited a striking reduction in dendritic complexity with increasing maturity at 14 DIV (Figure 5A, B, Two-way ANOVA ($p < 0.001$)). The number of dendritic branch points in Tau35 neurons decreased by 44% and the mean dendrite length reduced by 20% compared to WT neurons at 14 DIV, without any change in soma area (Figure 5C). Correct formation of the dendritic arbor has important consequences for synaptic function in neurons. Therefore, this marked reduction in dendritic complexity in hippocampal neurons suggests that the presence of Tau35 could result in decreased synaptic activity and/or synaptic strength.

Next, we used cultured hippocampal neurons to examine whether Tau35 affected dendritic spine morphology, since spine number and structure are known correlates of synaptic strength (Berry and Nedivi, 2017; Yuste and Bonhoeffer, 2001). The number of each morphological type of dendritic spine was analyzed from three-dimensional reconstructions of eGFP-expressing Tau35 and WT hippocampal neurons at 14 DIV

(Figure 5D). Overall dendritic spine density was reduced by 59% in Tau35 in comparison to WT neurons (Figure 5D). Notably, Tau35 expression in hippocampal neurons also affected the proportions of stubby and mushroom spines, both of which were significantly reduced (Figure 5D). This dramatic fall in the number of dendritic spines, coupled with selective decreases in the contributions of stubby and mushroom spines to the total spine pool, suggests that Tau35 expression is likely to have a negative impact on synaptic plasticity (Herms and Dorostkar, 2016), and could enhance synaptotoxicity.

Ultrastructural changes in hippocampal presynaptic terminals of Tau35 mice

To characterize the possible impact of Tau35 on presynaptic structure in the hippocampal CA1 region in mice, we adopted an ultrastructural approach (Figure 6A, B). At 4 months of age, there was a significant reduction (22%) in the number of synaptic vesicles per synapse in Tau35 hippocampus (Figure 6C). By 10 months of age, this genotypic difference was even more pronounced with synaptic vesicle density further reduced in Tau35 mice (39% lower than in WT mice) (Figure 6C). Similarly, the density of synaptic terminals in Tau35 mice was also reduced at both ages examined (Figure 6C). Tau35 mice harbored 38% fewer synapses/μm^2 compared to WT mice at 4 months and synaptic density diminished to 47% of WT at 10 months of age. In contrast, there were no significant differences in the presynaptic area or in the diameter of synaptic vesicles (Figure 6C), or in the percentage of docked synaptic vesicles (Figure S5A) in Tau35 mice in either age group. These findings signify that Tau35 has a marked and sustained negative impact on synaptic integrity and strength and that these detrimental effects progress further with aging.

We next carried out a detailed spatial analysis of the organization of synaptic vesicles in individual synapses from Tau35 and WT mice based on a randomly selected sample of representative middle sections through each terminal. A visually striking feature of synaptic clusters in Tau35 synapses is that the packing density of vesicles is significantly lower than in WT (Figure 7A, compare left and right panels). This was confirmed by quantifying vesicles per unit area using concave hulls to define cluster boundaries (4 months: WT, 1835 ± 97 vesicles/μm^2; Tau35, 1023 ± 55 vesicles/μm^2. Student's t-test, N=20 synapses, $p < 0.0001$.10 months: WT, 1208 ± 50 vesicles/μm^2; Tau35, 886 ± 51 vesicles/μm^2, Student's t-test, N=20 synapses, $p < 0.0001$). Next, we used the ultrastructural detail afforded by our method to investigate whether Tau35 influenced the physical positions of synaptic vesicles within the terminal architecture by mapping all vesicle coordinates with respect to the active zone center. The coordinates were used to generate color-coded mean spatial frequency distribution maps, revealing that Tau35 synapses had a lower density vesicle cloud behind the active zone than WT synapses at both ages (Figure 7B). Strikingly, difference plots for the Tau35 versus WT distribution maps show that vesicles in Tau35 synapses favor aggregation at sites adjacent to the active zone and at the lateral edges of the cluster (Figure 7B). Since these are likely regions for vesicle retrieval, it suggests a possible nanoscale correlate of recycling deficits at Tau35 terminals.

In addition to synaptic vesicle-driven fast transmission, slower synaptic signaling occurs via neuropeptides packaged in dense-core vesicles (DCVs). Therefore, we quantified the percentage of synapses harboring DCVs in Tau35 and WT mice. At 4 months of age, there was no difference between the genotypes (Figure S5B). However, 10 month-old Tau35 mice exhibited a 74% reduction in the percentage of hippocampal synapses harbouring DCVs (Figure S5B). This reduction in DCV-containing synapses in Tau35 mice occurs at a time when overt cognitive dysfunction and tauopathy are apparent in these animals, suggesting that the lack of synaptic DCVs could result in compromised release of neuropeptides and thereby further inhibit information transfer between synapses and neuronal connectivity.

Tau35 induces changes in EPSC kinetics without affecting synaptic vesicle pool sizes

We hypothesized that the changes observed in synaptic properties in Tau35 mice might have detrimental downstream consequences for information signaling. To investigate this idea, we recorded spontaneous neurotransmitter release using patch-clamp recording. Primary hippocampal neurons (11-16 DIV) from both WT and Tau35 mice exhibited spontaneous excitatory postsynaptic currents (sEPSCs) (Figure 8A). We found that Tau35 neurons exhibited a marked reduction of 77% in sEPSC frequency (Figure 8B), without changes in amplitude (data not shown), indicating an effect of Tau35 on the probability of presynaptic vesicle release. The half-width of sEPSCs in Tau35 neurons was increased more than two-fold (Figure 8B) and the rate of rise reduced to 43% of WT neurons (Figure 8B). To test the effect of Tau35 on the electrogenic properties of the neuronal plasma membrane, we evoked a series of action potentials (APs) and measured the waveform properties of the first AP evoked by a 300 pA, 500 ms square current injection (Figure S6A). None of the AP properties that were measured, including peak, threshold, maximum rate of rise, peak width, EPSC amplitude, time constant (tau), or rate of decay were affected by Tau35 (Figure S6A, B and data not shown). These data demonstrate that expression of Tau35 significantly influences EPSC kinetics, causing decreases in firing frequency and rate of rise and an increase in half-width. Asynchronous release of synaptic vesicles can result in delayed vesicle fusion at synaptic terminals, which profoundly affects the timing of sEPSCs (Chanaday et al., 2019; Chuhma and Ohmori, 1998). Therefore, our data suggest that the reduced frequency and increased half-width of sEPSCs caused by Tau35 may be due to asynchronous vesicle release from hippocampal neurons.

Synaptophysin-pHluorin (sypHy) was used as a probe to compare the sizes of the readily releasable and recycling pools of synaptic vesicle pools upon electrical and chemical stimulation of WT and Tau35 neurons (14-16 DIV). Although there appeared to be modest reductions in the proportions of both the readily releasable (from 13% to 9%) and recycling (from 30% to 22%) pools of synaptic vesicles in Tau35 hippocampal neurons (Figure S6C), these changes were not statistically significant. We conclude that Tau35 does not cause a marked switch in the magnitude of the readily releasable and recycling pools of synaptic vesicles in cultured hippocampal neurons.

Discussion

Proper maintenance of synaptic structure and function is critical for cognitive processing, and synaptic dysfunction is an early correlate of dementia and related tauopathies (Spires-Jones and Knafo, 2012). Axonal tau normally stabilizes the microtubule cytoskeleton in the presynaptic neuron, supporting vesicle trafficking and facilitating synaptic activity (Zhou *et al.*, 2017). Several studies have shown that trans-synaptic spreading of abnormal tau species may underlie the development of tauopathy (DeVos *et al.*, 2018; Liu *et al.*, 2012; Wegmann *et al.*, 2019). Furthermore, aberrant redistribution of phosphorylated tau to dendrites (Gotz *et al.*, 1995; Harris *et al.*, 2012; Ittner *et al.*, 2010; Tai *et al.*, 2012) and tau-induced relocation of the axon initial segment (Hatch *et al.*, 2017), result in excitotoxicity, synaptic depression and spine loss due to destabilization of the dendritic cytoskeleton (Ittner and Ittner, 2018). Similarly, tau fibrillization selectively increases the expression of postsynaptic receptors (Shrivastava *et al.*, 2019). However, the molecular mechanisms that underlie the synaptic damage caused by tau deposition are not understood. Here we report selective increases in the expression of HCN1 and HCN3 ion channels, accompanied by an array of dendritic and synaptic changes in Tau35 mice, a model of sporadic tauopathies, which include progressive supranuclear palsy, frontotemporal dementia and corticobasal dementia (Bondulich *et al.*, 2016).

HCN channels regulate a range of cellular properties, including membrane resistance, intrinsic membrane excitability and synaptic integration (Shah, 2014), and are emerging as key players in the pathogenesis of several neurodegenerative diseases (Chang *et al.*, 2019). In Tau35 primary hippocampal neurons, increases in I_h-dependent sag appeared in parallel with significant increases in the expression of HCN1 and HCN3 currents, in the absence of any changes in HCN2 and HCN4 channels, suggesting selective modulation of HCN channels due to expression of truncated tau. Increases in the expression of HCN1 and HCN3 channels were also observed in the brain of Tau35 mice. Impaired trafficking of HCN1 channels to distal dendrites or increased HCN expression (Musial *et al.*, 2018) is associated with increased I_h-dependent sag potential in rTg4510 mice that express mutant P301L tau (Booth *et al.*, 2016a; Crimins *et al.*, 2012). These differential changes in HCN channels in Tau35 mice suggest that specific presynaptic HCN channels might regulate synaptic communication and vesicle release in hippocampal Tau35 neurons, potentially by altering the interactions between synaptic vesicles and calcium channels (Huang *et al.*, 2017; Huang *et al.*, 2011).

In the hippocampus of young Tau35 mice, we found marked reductions in synapse density and in the number of synaptic vesicles in each synaptic terminal, changes that precede the appearance of overt tau pathology in these animals (Bondulich *et al.*, 2016). We also observed changes in the presynaptic cytoarchitecture in brains of young Tau35 mice. Whereas the majority of synaptic vesicles in WT mice were closely apposed to the active zone, synaptic vesicles in Tau35 mice were more loosely distributed without a prominent core cluster, aggregating instead at sites adjacent to the active zone and at the lateral edges of the cluster. Vesicle organization at presynaptic terminals of hippocampal synapses has been linked to synaptic efficacy (Marra *et al.*, 2012; Rey *et al.*, 2020; Rey *et al.*, 2015), suggesting that disrupting the integrity of

synaptic vesicle clusters could underlie deficits in synaptic signaling in Tau35 mice. In *Drosophila*, distinct states of the active zone have been proposed to regulate neuronal communication by modulating synaptic vesicle positioning and release (Kittel and Heckmann, 2016). Within a given synapse, not all release sites are equally re-used during sustained synaptic activity (Kusick *et al.*, 2020). The reduction in synaptic vesicles located at the active zone in Tau35 mouse brain may indicate disruption of synchronous vesicle release. The size and kinetics of synaptic vesicle pools also influences synaptic efficiency (Rey *et al.*, 2020). In the case of Tau35 synapses, lack of available synaptic vesicles could be a rate-limiting factor that contributes to reductions in the number of functional synapses and synaptic strength. Thus, it is plausible that Tau35, and potentially other truncated tau species, could interfere with the lateral movement or positioning of synaptic vesicles, ion channels and/or membrane components during sustained synaptic activity, resulting in reduced synaptic efficacy and contributing to cognitive decline (Atwood and Karunanithi, 2002; Hua *et al.*, 2013; Neher, 2010).

Expression of the disease-associated P301L tau mutation in rTg4510 transgenic mice, results in a robust reduction in dendritic arborization (Crimins *et al.*, 2012). Similar decreases in dendritic branching were observed during advanced tauopathy in Tau35 mice at 10 months of age. This Tau35-mediated reduction in dendritic branching is accompanied by progressive presynaptic changes, including reductions in the densities of both synaptic vesicles and synapses. Our findings have important mechanistic implications for disease because dendritic arborization influences the generation of new synapses, neuronal function, and cognitive performance, all of which are impaired in tauopathy. Dendrites are also a major source of neuropeptides and their release, even independently of electrical activity, enables sustained re-organization of neuronal networks (Ludwig and Leng, 2006). We observed a marked reduction in the percentage of synapses harboring DCVs in the hippocampus of aged Tau35 mice. These results mirror the reduction in DCV peptide density reported in the hippocampus in Alzheimer's disease (Marksteiner *et al.*, 2002). Taken together, our data suggest that expression of Tau35 damages synaptic cytoarchitecture and that this is likely to have significant negative impacts on neuronal connectivity and signaling.

To determine how the structural changes in synapses affect synaptic plasticity and function, we examined dendritic spine morphology in Tau35 cultured hippocampal neurons, since activity-dependent spine remodeling is critical for neuronal communication (Chater and Goda, 2014). Previous studies have demonstrated that synaptic strength is regulated by the number and size of individual dendritic spines (Berry and Nedivi, 2017; Yuste and Bonhoeffer, 2001). Tau35 hippocampal neurons exhibit a reduced density of dendritic spines, and smaller proportions of stubby and mushroom spines, whereas thin spines were unchanged. These results demonstrate that Tau35 expression results in the loss of mature spines, adversely affecting synaptic strength and further supporting the view that tau truncation is detrimental to both the structure and function of synapses.

Reduced dendritic and synaptic complexity have been linked to altered resonance in hippocampal pyramidal neurons of rTg4510 mice (Booth *et al.*, 2016a; Crimins *et al.*, 2012). Notably, we previously reported changes in resonance in Tau35 mice, including a reduction in impedance in older animals upon injection of an oscillating current (Tamagnini *et al.*, 2017). Here, we characterized the electrophysiological properties of Tau35 primary hippocampal neurons. We observed altered membrane electrical behavior in Tau35 neurons and identified increased voltage-sensitivity of non-inactivating potassium channels as a possible cause of the decreased impedance and voltage-dependent input resistance caused by Tau35 expression. Conversely, Tau35 hippocampal neurons did not exhibit changes in either input resistance or biophysical properties of voltage-gated potassium channels, that generate M-currents (I_M) (Wang *et al.*, 1998). However, we did detect increased I_h-dependent sag of the V_m deflection upon injection of negative current, paralleled by elevated expression of I_h-generating HCN1 and HCN3 channels. Interestingly, both I_h and I_M play critical roles in regulating plasma membrane excitability in the presence of oscillating potentials, driving neuronal resonance. The interplay of I_h and I_M has recently been reported to regulate intrinsic neuronal excitability and to affect disease progression in a SOD1^{G93A} mouse model of amyotrophic lateral sclerosis (Buskila *et al.*, 2019). Neurons with strong I_h currents are good resonators and operate as bandwidth filters (Boehlen *et al.*, 2013; Hu *et al.*, 2016). In contrast, inhibition of I_h and increased I_M results in low resonance, causing the neuron to function as a low-pass filter and attenuating higher frequencies (Hu *et al.*, 2002). Our data demonstrate that Tau35 is associated with increased I_h-related events in primary hippocampal neurons, whereas in aged animals, Tau35 is associated with increased I_M (Tamagnini *et al.*, 2017). Any alteration to the I_h/I_M ratio caused by Tau35 expression could therefore interfere with intrinsic neuronal excitability and the ability of hippocampal neurons to respond to specific stimuli, further disrupting neuronal connectivity.

We also found that sEPSCs developed by Tau35 primary hippocampal neurons were less frequent, wider, and slower to rise than those of WT neurons. These currents reflect alterations in presynaptic glutamate release and subsequent activation of post-synaptic α-Amino-3-hydroxy-5-methyl-4-isoxazolepropionic acid (AMPA) and α-Amino-3-hydroxy-5-methyl-4-isoxazolepropionic acid (NMDA) receptors (Turrigiano and Nelson, 2004). Notably, fluctuation in the release of presynaptic vesicles has been reported to profoundly affect both the timing of sEPSCs (Chanaday *et al.*, 2019; Chuhma and Ohmori, 1998) and synaptic vesicle distribution along the active zone (Kusick *et al.*, 2020). The changes we observed in sEPSCs in Tau35 hippocampal neurons could, therefore, caused by asynchronous release of presynaptic vesicles.

In conclusion, this study identifies previously undescribed roles for HCN1 and HCN3 channels in the development and progression of tauopathy (Figure S7). Our results demonstrate that increased expression of HCN channels is likely responsible for the increased I_h in Tau35 neurons. Aberrant signaling coincides with changes in synaptic ultrastructure, reducing the density of synaptic terminals as well as the cluster density of synaptic vesicles in individual terminals, adversely affecting network connectivity. Importantly, Tau35 also disrupts synaptic vesicle positioning in synaptic terminals, resulting in excessive accumulation of synaptic vesicles in the peri-active zone. Thus,

targeting specific HCN channels with pharmacological agents could potentially protect synapses and prevent disease progression in human tauopathy.

Materials and Methods

Ethics statement

All procedures were carried out in accordance with the Animals (Scientific Procedures) Act, 1986, following approval by the local ethical review committee. Procedures conformed to the ARRIVE guidelines.

Animals

Tau35 mice were generated by targeted knock-in to the *Hprt* locus under the control of the human tau promoter as described previously (Bondulich et al, 2016).

Preparation of mouse brain homogenates for western blots

Mice were sacrificed by cervical dislocation. Brains were removed and snap-frozen in dry-ice and stored at -80°C. Tissue was lysed by ultrasonication in ice-cold RIPA buffer (150 mM NaCl, 1 mM ethylenediaminetetraacetic acid [EDTA], 50mM Tris-HCl, 1% (v/v) NP-40, 1% (w/v) sodium deoxycholate, 0.5% (w/v) sodium dodecyl sulfate [SDS]), supplemented with protease inhibitor cocktail (cOmplete™, EDTA-free, Merck Millipore) and phosphatase inhibitor (PhosSTOP, Sigma-Aldrich) for 30 s at 40 kHz, incubated for 2 min on ice, repeating this cycle three times. Lysed tissue was centrifuged at 10,000g for 15 min at 4°C and the supernatants were stored at -20°C.

Western blots

Protein concentration was determined using a bicinchoninic acid protein assay, according to the manufacturer's instructions (Pierce™ BCA Protein Assay Kit, cat number: 23225, Thermo Scientific). Samples were prepared in Laemmli buffer and incubated at 95°C for 10 min. Samples were electrophoresed on 10% (w/v) SDS-polyacrylamide gels. Separated proteins were transferred to polyvinylidene difluoride (PVDF) membranes, blocked in Intercept® (TBS) Blocking Buffer (LI-COR Biosciences) and incubated in primary antibodies (Table 1), overnight at 4°C. Following washing in Tris-buffered saline containing 0.02% (w/v) Tween 20, membranes were incubated with appropriate fluorophore-conjugated secondary antibodies (Table 1) for antigen detection and imaged (Odyssey® imager, LI-COR Biosciences). ImageStudio™ Lite software (LI-COR Biosciences) was used for quantification of western blots.

Cell culture

Primary hippocampal neurons were prepared from embryonic (E) day 16.5-18.5 Tau35 and wild-type (WT) mice (Bondulich *et al.*, 2016). and cultured as described previously (Giacomini *et al.*, 2018). Neurons were transfected (Lipofectamine 2000, Thermo Fisher Scientific) with enhanced green fluorescent protein (eGFP) at 4-7 DIV and fixed at 14 DIV to monitor dendritic branching and to quantify spine density. Neurons were also cultured for 6, 9 and 14 DIV and either fixed in 4% (w/v) paraformaldehyde (PFA) and labelled with antibodies for immunofluorescence or lysed for analysis on western blots. For immunofluorescence staining, after removal of residual PFA, cells were permeabilized (0.5% Triton X-100) and incubated with primary antibodies overnight at 4°C, followed by incubation with Alexa–conjugated secondary antibodies. Before mounting (fluorescence mounting medium, Agilent), neurons were counterstained with 4′,6-diamidino-2-phenylindole (DAPI (300nM in PBS), Sigma). For blocking peptide

experiments, ten times excess of blocking peptide to antibody was used and samples were incubated overnight at 4°C.

Preparation of mouse brain tissue for immunolabeling and Golgi-Cox staining
Mice were sacrificed using terminal anaesthesia, perfused with phosphate buffered saline (PBS) and post-fixed in 4% (w/v) PFA overnight at 4°C. Brain sections (50-200 µm) were prepared using a vibratome (VT1000 S Vibrating blade microtome, Leica Biosystems) and stored free-floating in 30% (v/v) ethylene glycol, 15% (w/v) sucrose in PBS at −20°C.

For immunofluorescence, 50 µm sections were washed in PBS, blocked in 3% (v/v) goat (Sigma) or horse serum (Sigma), in 0.5% (w/v) Triton X-100 in PBS, and incubated in primary antibody (Table 1) for 24 h at 4°C. After washing, sections were incubated in the appropriate fluorophore-conjugated secondary antibody (Table 1) for 4-6 h at 4°C, and counterstained with DAPI, before mounting in fluorescence mounting medium (Agilent).

For Golgi-Cox staining, 200 µm sections were stained according to the manufacturer's instructions (sliceGolgi Kit, Bioenno Lifesciences) and imaged using a Nikon Ti-E two-camera microscope (×60, 1.4 NA, oil objective). Three-dimensional digital reconstruction of dendritic, axonal and spine structures was performed using Neurolucida software (BFM Bioscience). Whole brain sections were imaged using a slide scanner (VS120EL100W, Virtual Slide Microscope, Olympus) equipped with x20, 0.75 NA and x40, 0.95 NA, air objectives.

Preparation of mouse brain for ultrastructural analysis
Mice were sacrificed using terminal anaesthesia, perfused with PBS and post-fixed in 4% (w/v) PFA, 0.1% (w/v) glutaraldehyde in PBS, overnight at 4°C. Brains were removed and 300 µm transverse brain sections were prepared using a vibratome (VT1000 S Vibrating blade microtome, Leica Biosystems). Fixative was replaced with 0.2 M sodium cacodylate and 0.2 M sodium cacodylate, supplemented with 0.02 M $CaCl_2$. Sections were treated with 2% (w/v) osmium tetroxide for 1 h on ice. After washing in ultra-pure water, sections were stained for 20 min in 0.1% (w/v) thiocarbohydrazide at ambient temperature, followed by three washes in water. Sections were then treated with 2% (w/v) osmium tetroxide in 0.2 M sodium cacodylate, supplemented with 0.02 M $CaCl_2$ and 1.5% (w/v) potassium ferrocyanide. After a further water wash, sections were stained by incubating in 1% (w/v) uranyl acetate overnight at 4°C. Stained sections were dehydrated in ascending concentrations of ethanol, then in acetone, before flat embedding in ascending concentrations of Durcupan resin (25% [v/v] for 2 h, 50% [v/v] for 2 h, 70% [v/v] for 2 h, 100% [v/v] overnight). Fresh resin was added and polymerised using a UV light translinker for 3-4 days at 4°C (UVP TL-2000 Translinker). The stained and embedded hippocampus was dissected, glued onto a BEEM capsule, mounted in an ultramicrotome (Leica), and ultrathin 70 nm sections were collected on hexagonal 300-mesh nickel grids (3.05 mm; Agar Scientific).

Negative-stain transmission electron microscopy
Transmission electron microscopy projection images were collected using a JEM1400-Plus microscope (JEOL) operated at 100 kV and equipped with a Gatan OneView camera (4k 9 4k). High magnification (20,000x) and panoramic (5,000x) micrographs were obtained for synaptic vesicle and synapse density analyses, respectively. Only synapses with defined postsynaptic densities and containing between 10-200 synaptic vesicles, were imaged for ultrastructural analysis. Synaptic vesicles and synapses were manually counted in blinded coded images to avoid bias. Synaptic vesicle diameter and presynaptic area were measured using ImageJ. For three-dimensional reconstructions, serial micrographs were aligned using Reconstruct software.

Functional assessment of the presynaptic vesicle pool
For high-sensitivity readouts of functional synapses and presynaptic vesicle pool sizes, we used 14-16 DIV hippocampal neuronal cultures, prepared from E16.5-18.5 Tau35 and/or control mice. Presynaptic vesicles were labelled by transduction with pAAV6-sypHy1x (sypHy) vector at 7 DIV and imaging was performed at 14-16 DIV to allow time for viral expression. An Olympus BX61WI microscope (× 60, 1.0 NA, dipping objective, excitation: 480/20, emission: 520/35) attached to an Andor Ixon+ electron multiplying charge-coupled device camera (4 × 4 binning, 12.5 Hz acquisition) controlled by custom-written Micromanager routines was used for imaging. Experiments were performed in pre-warmed Extracellular Bath Solution (EPS) (136 mM NaCl, 2.5 mM KCl, 10 mM HEPES (pH 7.4), 1.3 mM $MgCl_2$, 10 mM D-Glucose, 2 mM $CaCl_{3)}$, supplemented with 20 mM 6-cyano-7-nitroquinoxaline-2,3-dione (CNQX) and 50 mM (2*R*)-amino-5-phosphonovaleric acid; (2*R*)-amino-5-phosphonopentanoic acid (APV) to block AMPA and NMDA receptor responses, respectively. Transduced neurons were stimulated with 40 AP at 20 Hz, to generate a readout of readily releasable pool size, followed by a single 600 AP, 20 Hz stimulation in the presence of 1μM bafilomycin A1 (Sigma-Aldrich), to induce alkaline trapping and lock presynaptic vesicles in an alkaline state. The total synaptic vesicle pool population was visualized by replacing EBS-baf with NH_4Cl solution (50 mM NH_4Cl, 86 mM NaCl, 2.5 mM KCl, 10 mM HEPES, 1.3 mM $MgCl_2$, 10 mM D-Glucose, 2 mM $CaCl_2$ (pH7.4)). Selection of regions of interest (Dorostkar *et al.*, 2010) and data analysis was performed using custom built routines and scripts in Igor Pro (Wavemetrics).

Patch-clamp recording of cultured hippocampal neurons
Neurons were cultured on 13 mm coverslips as previously described (Giacomini *et al.*, 2018). Immediately prior to recording, coverslips were transferred to a submerged-style recording chamber where they were continuously perfused (1-3 ml/min) with Carbogen (95% O_2, 5% CO_2), artificial cerebrospinal fluid (aCSF, 124 mM NaCl, 3 mM KCl, 24 mM $NaHCO_{3,}$ 2 mM $CaCl_{2,}$ 1.25 mM NaH_2PO_4, 1 mM $MgSO_4$, 10 mM D-glucose) maintained at 34°C with a temperature control system (Scientifica, UK). Neurons were visualized with an infrared, differential interference contrast microscope (Scientifica, UK). Borosilicate glass micropipettes were pulled with a horizontal puller (Sutter, USA) to an access resistance of 5-9 MΩ. Single micropipettes were filled with intracellular solution (120 mM K-gluconate, 10 mM Na_2-phosphocreatine, 0.3 mM Na_2-GTP, 10 mM HEPES, 4 mM KCl, 4 mM Mg-ATP, pH 7.2, 280-290 mOsm). Some recordings were conducted

in the presence of Alexa Fluor™ 488 dye (30 μM) in the intracellular solution. Following the clamping of a stable whole-cell configuration, the junction potential V_j = 15 mV arose due to the difference in composition between intracellular and extracellular solutions; this was corrected for arithmetically during analysis. All signals were amplified with a Multiclamp 700B amplifier and digitized using a Digidata 1550B. For whole cell recordings, a hyperpolarizing current (500 ms, -100 pA) was injected and the consequent plasma membrane voltage (V_m) deflection was measured. To avoid the possibility of bias arising from cell-to-cell variability of the resting membrane potential, all recordings were conducted in the presence of a constant current, holding the pre-stimulus at V_m = -80 mV. For voltage-clamp recording of sEPSCs, a gap-free protocol at a holding potential V_h = -70 mV was used. Data analysis for quantifying the frequency and the waveform properties of sEPSCs used Clampfit (Molecular Devices, USA). The template search analysis tool embedded in Clampfit was used to identify single sEPSCs for each cell, with a manual check to identify any false positives and negatives. The average frequency was calculated as the number of events detected during 30 s, expressed in Hz. Averaged sEPSCs from all detected events were used to measure sEPSC waveform properties in each cell. Analysis tools in Clampfit were used to quantify the sEPSC rate of rise, peak, and halfwidth. Current-Voltage (I-V) curves for voltage-gated, non-inactivating, outward currents were carried out as follows. Series resistance was compensated for (10%-95% correction) and the capacitance of the pipette neutralized. Outward, non-inactivating, voltage gated currents were evoked by applying n=12, 30 ms, 10 mV voltage steps, starting from an initial V_h of -90 mV. Each recorded current was leak subtracted and normalized to membrane capacitance to measure the specific current. The specific conductance (G) was calculated as the ratio between the specific current and the electrochemical force for potassium (E_K = 100 mV). Cell-to-cell Boltzmann sigmoidal fit was used to estimate the maximal specific conductance (Gmax) and the half-activation voltage ($V_{1/2}$) for each neuron. Current clamp recordings used a set pre-stimulus V_m of -80 mV, with a constant current injection (apart from recording the resting membrane potential). Passive electrical properties were measured by injecting a -100 pA, 500 ms square current step. The voltage deflection caused by this current injection followed a single exponential decay function. The steady state voltage deflection (A) and the voltage extrapolated *ad infinitum* (B) for a single exponential function fit between 10% and 90% of the minimum point (C) of the voltage deflection, were used to calculate cell input resistance (R_{in}) and sag. Sag_{sub} was calculated as (C-A)/C and sag_{fit} was calculated as (B-A)/B and expressed as a percentage. Sag was measured as subtraction of the negative peak (sag_{sub}) and of the extrapolated first exponential fit of the Vm decay (sag_{fit}) upon the injection of a hyperpolarizing step (Tamagnini *et al.*, 2015).

Statistical analysis

Statistical analyses were performed using GraphPad Prism. Student's t-test, one-way or two-way analysis of variance was used to determine differences between groups. Each experiment was performed at least in triplicate, as indicated.

Author Contributions

DG, FT, LB, SLR, SU, SJP, HS performed the experiments.

DG, FT, SLR, HS performed data analysis.
KF, LB, KS advised on data analysis.
DPH, KS, LCS, WN supervised the project
DG, DPH, FT, KS, WN wrote and edited the manuscript.

Acknowledgments

This work was supported by grants from the Alzheimer's Society and the Alzheimer's Research UK King's College London Network Centre to DG, WN and DPH, and the BBSRC to KS. We thank the late Professor Peter Davies (Feinstein Institute for Medical Research, USA) for generously providing the PHF1 antibody used in this study.

Table 1: Antibodies

REAGENT	SOURCE	IDENTIFIER
Phosphorylated tau Mouse monoclonal	Peter Davies (Feinstein Institute for Medical Research, USA)	PHF1 (Ser396/404)
HCN1 (clone N70/28) Mouse monoclonal	Merck Millipore	Cat# MABN20, RRID: AB_10806489
HCN1 Rabbit polyclonal	Alomone Labs	Cat# APC-056, RRID: AB_2039900
HCN1 Guinea pig polyclonal	Alomone Labs	Cat# AGP-203, RRID: AB_2756625
HCN2 (clone S71/37) Mouse monoclonal	Novus Biologicals	Cat# NBP2-12895, RRID: AB_10682868
HCN2 Rabbit polyclonal	Alomone Labs	Cat# APC-030, RRID: AB_2313726
HCN3 Rabbit polyclonal	Alomone Labs	Cat# APC-057, RRID: AB_2039904
HCN3 Rat monoclonal	Santa Cruz Biotechnology	Cat# Sc-58621, RRID: AB_783695
HCN4 Guinea pig polyclonal	Alomone Labs	Cat# AGP-004, RRID: AB_2340957
GAPDH (clone 6C5) Mouse monoclonal	Santa Cruz Biotechnology	Cat# Sc-32233 RRID: AB_627679
Goat anti-mouse IgG (H+L) Alexa Fluor 488	ThermoFisher Scientific	Cat# A-11001, RRID: AB_2534069
Goat anti-rabbit IgG (H+L) Alexa Fluor 546	ThermoFisher Scientific	Cat# A-21085, RRID: AB_2535742
Goat anti-guinea pig IgG (H+L) Alexa FluorA ® 488-AffiniPure	Jackson ImmunoResearch Laboratories Inc	Cat# 106-545-003-JIR, RRID: AB_2337438
Goat anti-mouse IgG IRDye™ 680	Li-Cor Biosciences	Cat# 926-68070, RRID: AB_10956588
Goat anti-rabbit IgG IRDye™ 800	Li-Cor Biosciences	Cat# 926-32211, RRID: AB_621843

Figure Legends

Figure 1. Tau Phosphorylation and HCN Channel Expression are Increased in Tau35 Mouse Brain
Western blots of brain homogenates from wild-type (WT) and Tau35 mice aged (A, C) 4 or (B, D) 10 months, probed with antibodies to (A, B) phosphorylated tau (PHF1), total tau, (C, D) HCN1 or HCN3, and glyceraldehyde 3-phosphate dehydrogenase (GAPDH). Quantification of the blots is shown in the graphs as mean ± SEM; n= 7. Student's t-test, *$p < 0.05$, **$p < 0.01$.

Figure 2. Tau Phosphorylation and HCN Channel Expression are Increased in Tau35 Primary Hippocampal Neurons
Western blots of lysates of primary hippocampal neurons (14 DIV) from wild-type (WT) and Tau35 mice, probed with antibodies to (A) phosphorylated tau (PHF1) and total tau, (B) HCN1 (left) or HCN3 (right), and glyceraldehyde 3-phosphate dehydrogenase (GAPDH). Quantification of the blots is shown in the graphs as mean ± SEM; n=4-6. Student's t-test, *$p < 0.05$, **$p < 0.01$. (C) Immunofluorescence labeling of WT and Tau35 mouse hippocampal neurons at 14 DIV with HCN1 and HCN3 antibodies, and DAPI staining of nuclei (scale bars: 50μm). Graphs show quantification of mean fluorescence intensity (± SEM) of HCN1 (left) and HCN3 (right). Student's t-test, n=150 (WT) and n=120 (Tau35) neurons, from 3 independent experiments. *$p < 0.05$, **$p < 0.01$.

Figure 3. I_h-Dependent Sag and Excitatory Neurotransmission are Altered in Tau35 Primary Hippocampal Neurons
(A) Average traces ± SEM boundaries of V_m hyperpolarization by injection of -100 pA, 500 ms current in wild-type (WT) and Tau35 mouse hippocampal neurons (11-16 DIV). (B) Graphs show sag_{sub}, sag_{fit}, and rebound potential. Graphs show quantification of the mean ± SEM; n=8 (WT) and n=11 (Tau35) neurons. Student's t-test, *$p < 0.05$, **$p < 0.01$.

Figure 4. Progressive Loss of Dendritic Complexity, Presynaptic Vesicles and Synapses in Tau35 Mouse Brain
(A) Images of Golgi-Cox stained wild-type (WT) and Tau35 CA1 hippocampal neurons in mice (10 months). Scale bars 10μm. (B) Sholl analysis illustrates reduced dendritic complexity in Tau35 mouse hippocampus. Graph shows quantification of the mean ± SEM. Two-way ANOVA, n=40 neurons from 6 mice of each genotype. (C) Graphs showing the number of primary branch points per neuron, mean dendrite length, and soma area in CA1 neurons of WT and Tau35 mice aged 10 months. Student's t-test, n=40 neurons from 6 mice of each genotype. * $p < 0.05$.

Figure 5. Reduced Dendritic Branching and Spine Density in Tau35 Primary Hippocampal Neurons
(A) Fluorescent images (left) and Neurolucida drawings (right) of wild-type (WT) and Tau35 primary hippocampal neurons, transfected at 4 days *in vitro* (DIV) with a plasmid expressing enhanced green fluorescent protein (eGFP) and imaged at 14 DIV. Scale

bars 50μm. (B) Sholl analysis of dendritic branching in WT and Tau35 hippocampal neurons at 14 DIV shows reduced dendritic complexity in Tau35 neurons. Graph shows quantification of the mean ± SEM. Two-way ANOVA ($p < 0.001$) n=52 neurons of each genotype from 4-5 independent experiments. (C) Graphs showing the number of dendritic branch points, mean dendrite length, and soma area in WT and Tau35 hippocampal neurons at 14 DIV. Student's t-test, n=52 neurons of each genotype, from 4-5 independent experiments. (D) Representative fluorescent images of dendrites from WT and Tau35 hippocampal neurons transfected with a plasmid expressing eGFP and imaged at 14 DIV. Stubby spines (yellow), thin spines (blue) and mushroom spines (red) are indicated. Graphs show the number of spines/μm dendrite length and the percentage of each spine type in WT and Tau35 hippocampal neurons at 14 DIV. Student's t-test, n=50 neurons of each genotype from 4 independent experiments. * $p < 0.05$, ** $p < 0.01$.

Figure 6. Ultrastructural Analysis of Synapses in Wild-Type and Tau35 Mouse Brain

(A) Representative electron micrographs of CA1 synapses of wild-type (WT) and Tau35 mice aged 4 months (left) and 10 months (right). Presynaptic (blue) and postsynaptic (green) structures, and synaptic vesicles (red) are pseudocoloured, as indicated. Scale bars: 100 nm. (B) Electron micrographs (left) and 3D serial reconstructions (right) of WT and Tau35 CA1 hippocampal synapses in mice aged 4 months. Presynaptic (light blue) and postsynaptic (pink) structures are separated by the electron-dense active zone (green), which is surrounded by synaptic vesicles (white). Mitochondria are shown in red. Scale bars 100 nm. (C) Graphs showing the number of synaptic vesicles (SVs) per synapse, synaptic density, SV diameter and presynaptic area of the CA1 region of the hippocampus in WT and Tau35 mice aged 4 and 10 months. Two-way ANOVA, n=100-150 synapses from 3 mice of each genotype. * $p < 0.05$, ** $p < 0.01$.

Figure 7. Synaptic Vesicle Organization in Wild-Type and Tau35 Mice

(A) Schematics showing representative vesicle clusters in synaptic terminals in wild-type (WT) and Tau35 mice (4 and 10 months). Circles indicate individual synaptic vesicles; orange cross-hairs indicate active zone centers. Scale bars: 200 nm. (B) Color-coded heatmaps show mean vesicle density distributions for WT and Tau35 mice (4 and 10 months), n=20-21 synapses. Cross-hairs indicate active zone (AZ) centers. Scale bars: 200 nm. Vesicle density is significantly higher in WT mice at both ages, Student's t-test, $p < 0.0001$. Panels on right show difference images of signal predominating in WT (blue) and Tau35 (red) clusters.

Figure 8. Altered EPSC Kinetics in Tau35 Primary Hippocampal Neurons

(A) Spontaneous excitatory postsynaptic currents (sEPSCs) in wild-type (WT) and Tau35 hippocampal neurons (11-16 DIV). Left: representative traces; right, average traces ± SEM. (B) Graphs show frequency, half-width and rate of rise of sEPSCs (mean ± SEM), Student's t-test, n=8 (WT) and n=11 (Tau35) neurons. * $p < 0.05$, **** $p < 0.0001$.

References

Atwood, H.L., and Karunanithi, S. (2002). Diversification of synaptic strength: presynaptic elements. Nat Rev Neurosci 3 (7): 497-516.

Berry, K.P., and Nedivi, E. (2017). Spine Dynamics: Are They All the Same? Neuron96 (1): 43-55.

Boehlen, A., Henneberger, C., Heinemann, U., and Erchova, I. (2013). Contribution of near-threshold currents to intrinsic oscillatory activity in rat medial entorhinal cortex layer II stellate cells. J Neurophysiology. 109 (2): 445-463.

Bondulich, M.K., Guo, T., Meehan, C., Manion, J., Rodriguez Martin, T., Mitchell, J.C., Hortobagyi, T., Yankova, N., Stygelbout, V., Brion, J.P.*, et al.* (2016). Tauopathy induced by low level expression of a human brain-derived tau fragment in mice is rescued by phenylbutyrate. Brain. 139 (Pt8): 2290-2306.

Booth, C.A., Ridler, T., Murray, T.K., Ward, M.A., de Groot, E., Goodfellow, M., Phillips, K.G., Randall, A.D., and Brown, J.T. (2016a). Electrical and network neuronal properties are preferentially disrupted in dorsal, but not ventral, medial entorhinal cortex in a mouse model of tauopathy. J Neurosci 36 (2): 312-324.

Booth, C.A., Witton, J., Nowacki, J., Tsaneva-Atanasova, K., Jones, M.W., Randall, A.D., and Brown, J.T. (2016b). Altered intrinsic pyramidal neuron properties and pathway-specific synaptic dysfunction underlie aberrant hippocampal network function in a mouse model of tauopathy. J Neurosci 36 (2): 350-363.

Buskila, Y., Kekesi, O., Bellot-Saez, A., Seah, W., Berg, T., Trpceski, M., Yerbury, J.J., and Ooi, L. (2019). Dynamic interplay between H-current and M-current controls motoneuron hyperexcitability in amyotrophic lateral sclerosis. Cell Death Dis 10 (4): 310.

Chanaday, N.L., Cousin, M.A., Milosevic, I., Watanabe, S., and Morgan, J.R. (2019). The synaptic vesicle cycle revisited: new insights into the modes and mechanisms. J Neurosci 39(42): 8209-8216.

Chang, X., Wang, J., Jiang, H., Shi, L., and Xie, J. (2019). Hyperpolarization-activated cyclic nucleotide-gated channels: an emerging role in neurodegenerative diseases. Front Mol Neurosci 12: 141.

Chater, T.E., and Goda, Y. (2014). The role of AMPA receptors in postsynaptic mechanisms of synaptic plasticity. Front Cell Neurosci. 8: 401.

Chuhma, N., and Ohmori, H. (1998). Postnatal development of phase-locked high-fidelity synaptic transmission in the medial nucleus of the trapezoid body of the rat. J Neurosci 18 (1): 512-520.

Crespo-Biel, N., Theunis, C., and Van Leuven, F. (2012). Protein tau: prime cause of synaptic and neuronal degeneration in Alzheimer's disease. Int J Alzheimers Dis 2012: 251426.

Crimins, J.L., Rocher, A.B., and Luebke, J.I. (2012). Electrophysiological changes precede morphological changes to frontal cortical pyramidal neurons in the rTg4510 mouse model of progressive tauopathy. Acta neuropathol 124 (6): 777-795.

DeVos, S.L., Corjuc, B.T., Oakley, D.H., Nobuhara, C.K., Bannon, R.N., Chase, A., Commins, C., Gonzalez, J.A., Dooley, P.M., Frosch, M.P., and Hyman, B.T. (2018).

Synaptic tau seeding precedes tau pathology in human Alzheimer's disease brain. Front Neurosci 12: 267.
Dorostkar, M.M., Dreosti, E., Odermatt, B., and Lagnado, L. (2010). Computational processing of optical measurements of neuronal and synaptic activity in networks. J Neurosci Methods 188 (1): 141-150.
Gauthier-Kemper, A., Weissmann, C., Golovyashkina, N., Sebo-Lemke, Z., Drewes, G., Gerke, V., Heinisch, J.J., and Brandt, R. (2011). The frontotemporal dementia mutation R406W blocks tau's interaction with the membrane in an annexin A2-dependent manner. J Cell Biol. 192 (4): 647-661.
Giacomini, C., Koo, C.Y., Yankova, N., Tavares, I.A., Wray, S., Noble, W., Hanger, D.P., and Morris, J.D.H. (2018). A new TAO kinase inhibitor reduces tau phosphorylation at sites associated with neurodegeneration in human tauopathies. Acta Neuropathol. Commun. 6 (1): 37
Gotz, J., Probst, A., Spillantini, M.G., Schafer, T., Jakes, R., Burki, K., and Goedert, M. (1995). Somatodendritic localization and hyperphosphorylation of tau protein in transgenic mice expressing the longest human brain tau isoform. The EMBO J 14 (7): 1304-1313.
Gotz, J., Xia, D., Leinenga, G., Chew, Y.L., and Nicholas, H.R. (2013). What renders TAU toxic. Front Neurol 4: 72.
Guo, T., Noble, W., and Hanger, D.P. (2017). Roles of tau protein in health and disease. Acta Neuropathol 133 (5): 665-704.
Hall, A.M., Throesch, B.T., Buckingham, S.C., Markwardt, S.J., Peng, Y., Wang, Q., Hoffman, D.A., and Roberson, E.D. (2015). Tau-dependent Kv4.2 depletion and dendritic hyperexcitability in a mouse model of Alzheimer's disease. J Neurosci 35 (15): 6221-6230.
Hanger, D.P., Goniotaki, D., and Noble, W. (2019). Synaptic Localisation of Tau. Adv Exp Med Biol 1184: 105-112.
Harris, J.A., Koyama, A., Maeda, S., Ho, K., Devidze, N., Dubal, D.B., Yu, G.Q., Masliah, E., and Mucke, L. (2012). Human P301L-mutant tau expression in mouse entorhinal-hippocampal network causes tau aggregation and presynaptic pathology but no cognitive deficits. Plos One 7(9): e45881.
Hatch, R.J., Wei, Y., Xia, D., and Gotz, J. (2017). Hyperphosphorylated tau causes reduced hippocampal CA1 excitability by relocating the axon initial segment. Acta Neuropathol 133 (5): 717-730.
He, C., Chen, F., Li, B., and Hu, Z. (2014). Neurophysiology of HCN channels: from cellular functions to multiple regulations. Prog Neurobiol 112: 1-23.
Henstridge, C.M., Hyman, B.T., and Spires-Jones, T.L. (2019). Beyond the neuron-cellular interactions early in Alzheimer disease pathogenesis. Nat Rev Neurosci. 20 (2): 94-108.
Herms, J., and Dorostkar, M.M. (2016). Dendritic spine pathology in neurodegenerative diseases. Annu Rev Pathol 11: 221-250.
Hirokawa, N., Funakoshi, T., Sato-Harada, R., and Kanai, Y. (1996). Selective stabilization of tau in axons and microtubule-associated protein 2C in cell bodies and dendrites contributes to polarized localization of cytoskeletal proteins in mature neurons. J Cell Biol 132 (4): 667-679.

Hoover, B.R., Reed, M.N., Su, J., Penrod, R.D., Kotilinek, L.A., Grant, M.K., Pitstick, R., Carlson, G.A., Lanier, L.M., Yuan, L.L.*, et al.* (2010). Tau mislocalization to dendritic spines mediates synaptic dysfunction independently of neurodegeneration. Neuron 68 (6): 1067-1081.
Hu, H., Vervaeke, K., and Storm, J.F. (2002). Two forms of electrical resonance at theta frequencies, generated by M-current, h-current and persistent Na+ current in rat hippocampal pyramidal cells. J Physiol 545 (3): 783-805.
Hu, R., Ferguson, K.A., Whiteus, C.B., Meijer, D.H., and Araneda, R.C. (2016). Hyperpolarization-activated currents and subthreshold resonance in granule cells of the olfactory bulb. 3 (5) eNeuro.
Hua, Y., Woehler, A., Kahms, M., Haucke, V., Neher, E., and Klingauf, J. (2013). Blocking endocytosis enhances short-term synaptic depression under conditions of normal availability of vesicles. Neuron 80 (2): 343-349.
Huang, Z., Li, G., Aguado, C., Lujan, R., and Shah, M.M. (2017). HCN1 channels reduce the rate of exocytosis from a subset of cortical synaptic terminals. Scientific reports 7: 40257.
Huang, Z., Lujan, R., Kadurin, I., Uebele, V.N., Renger, J.J., Dolphin, A.C., and Shah, M.M. (2011). Presynaptic HCN1 channels regulate Cav3.2 activity and neurotransmission at select cortical synapses. Nat Neurosci. 14 (4): 478-486.
Ittner, A., and Ittner, L.M. (2018). Dendritic Tau in Alzheimer's Disease. Neuron 99 (1): 13-27.
Ittner, L.M., Ke, Y.D., Delerue, F., Bi, M., Gladbach, A., van Eersel, J., Wolfing, H., Chieng, B.C., Christie, M.J., Napier, I.A.*, et al.* (2010). Dendritic function of tau mediates amyloid-beta toxicity in Alzheimer's disease mouse models. Cell 142 (3): 387-397.
Jackson, J.S., Witton, J., Johnson, J.D., Ahmed, Z., Ward, M., Randall, A.D., Hutton, M.L., Isaac, J.T., O'Neill, M.J., and Ashby, M.C. (2017). Altered synapse stability in the early stages of tauopathy. Cell Rep 18 (13): 3063-3068.
Kittel, R.J., and Heckmann, M. (2016). Synaptic vesicle proteins and active zone plasticity. Front Synaptic Neurosci 8: 8.
Kneynsberg, A., Combs, B., Christensen, K., Morfini, G., and Kanaan, N.M. (2017). Axonal degeneration in tauopathies: disease relevance and underlying mechanisms. Front Neurosci 11: 572.
Kusick, G.F., Chin, M., Raychaudhuri, S., Lippmann, K., Adula, K.P., Hujber, E.J., Vu, T., Davis, M.W., Jorgensen, E.M., and Watanabe, S. (2020). Synaptic vesicles transiently dock to refill release sites. Nat Neurosci. 23 (11): 1329-1338
Liu, C., Song, X., Nisbet, R., and Götz, J. (2016). Co-immunoprecipitation with tau isoform-specific antibodies reveals distinct protein interactions and highlights a putative role for 2N tau in disease. J Biol Chem 291(15): 8173-8188.
Liu, L., Drouet, V., Wu, J.W., Witter, M.P., Small, S.A., Clelland, C., and Duff, K. (2012). Trans-synaptic spread of tau pathology in vivo. Plos One 7(2): e31302.
Lleo, A., Nunez-Llaves, R., Alcolea, D., Chiva, C., Balateu-Panos, D., Colom-Cadena, M., Gomez-Giro, G., Munoz, L., Querol-Vilaseca, M., Pegueroles, J.*, et al.* (2019). Changes in synaptic proteins precede neurodegeneration markers in preclinical Alzheimer's disease cerebrospinal fluid. Mol Cell Proteomics 18 (3): 546-560.
Ludwig, M., and Leng, G. (2006). Dendritic peptide release and peptide-dependent behaviours. Nat Rev Neurosci 7(2): 126-136.

Magee, J.C. (1999). Dendritic Ih normalizes temporal summation in hippocampal CA1 neurons. Nat Neurosci 2 (9): 848.
Marksteiner, J., Kaufmann, W.A., Gurka, P., and Humpel, C. (2002). Synaptic proteins in Alzheimer's disease. J Mol Neurosci 18 (1-2): 53-63.
Marra, V., Burden, J.J., Thorpe, J.R., Smith, I.T., Smith, S.L., Hausser, M., Branco, T., and Staras, K. (2012). A preferentially segregated recycling vesicle pool of limited size supports neurotransmission in native central synapses. Neuron 76 (3): 579-589.
McInnes, J., Wierda, K., Snellinx, A., Bounti, L., Wang, Y.C., Stancu, I.C., Apostolo, N., Gevaert, K., Dewachter, I., Spires-Jones, T.L.*, et al.* (2018). Synaptogyrin-3 mediates presynaptic dysfunction induced by tau. Neuron 97(4): 823-835 e828.
Moreno, H., Morfini, G., Buitrago, L., Ujlaki, G., Choi, S., Yu, E., Moreira, J.E., Avila, J., Brady, S.T., Pant, H.*, et al.* (2016). Tau pathology-mediated presynaptic dysfunction. Neuroscience 325: 30-8.
Musial, T.F., Molina-Campos, E., Bean, L.A., Ybarra, N., Borenstein, R., Russo, M.L., Buss, E.W., Justus, D., Neuman, K.M., Ayala, G.D.*, et al.* (2018). Store depletion-induced h-channel plasticity rescues a channelopathy linked to Alzheimer's disease. Neurobiol Learn Mem 154: 141-157.
Neher, E. (2010). What is rate-limiting during sustained synaptic activity: vesicle supply or the availability of release sites. Front Synaptic Neurosci 2: 144.
Paspalas, C.D., Wang, M., and Arnsten, A.F. (2013). Constellation of HCN channels and cAMP regulating proteins in dendritic spines of the primate prefrontal cortex: potential substrate for working memory deficits in schizophrenia. Cereb Cortex 23 (7): 1643-1654.
Peng, Y.R., He, S., Marie, H., Zeng, S.Y., Ma, J., Tan, Z.J., Lee, S.Y., Malenka, R.C., and Yu, X. (2009). Coordinated changes in dendritic arborization and synaptic strength during neural circuit development. Neuron 61 (1): 71-84.
Pooler, A.M., Noble, W., and Hanger, D.P. (2014). A role for tau at the synapse in Alzheimer's disease pathogenesis. Neuropharmacology 76 Pt A:1-8.
Rey, S., Marra, V., Smith, C., and Staras, K. (2020). Nanoscale remodeling of functional synaptic vesicle pools in Hebbian plasticity. Cell Rep 30 (6): 2006-2017 e3.
Rey, S.A., Smith, C.A., Fowler, M.W., Crawford, F., Burden, J.J., and Staras, K. (2015). Ultrastructural and functional fate of recycled vesicles in hippocampal synapses. Nat Commun. 6: 8043.
Richter, H., Heinemann, U., and Eder, C. (2000). Hyperpolarization-activated cation currents in stellate and pyramidal neurons of rat entorhinal cortex. Neurosci Lett 281 (1): 33-36.
Scheff, S.W., Price, D.A., Schmitt, F.A., and Mufson, E.J. (2006). Hippocampal synaptic loss in early Alzheimer's disease and mild cognitive impairment. Neurobiol Aging 27 (10): 1372-1384.
Shah, M.M. (2014). Cortical HCN channels: function, trafficking and plasticity. J. Physiol. 592 (13): 2711-2719.
Shaw, A.S., and Filbert, E.L. (2009). Scaffold proteins and immune-cell signalling. Nat Rev Immunol 9 (1): 47-56.
Shrivastava, A.N., Redeker, V., Pieri, L., Bousset, L., Renner, M., Madiona, K., Mailhes-Hamon, C., Coens, A., Buee, L., Hantraye, P.*, et al.* (2019). Clustering of tau fibrils

impairs the synaptic composition of alpha3-Na(+)/K(+)-ATPase and AMPA receptors. EMBO J 38 (3):e99871
Spires-Jones, T., and Knafo, S. (2012). Spines, plasticity, and cognition in Alzheimer's model mice. Neural Plast 2012: 319836.
Stefanoska, K., Volkerling, A., Bertz, J., Poljak, A., Ke, Y.D., Ittner, L.M., and Ittner, A. (2018). An N-terminal motif unique to primate tau enables differential protein-protein interactions. J Biol Chem 293 (10): 3710-3719.
Sudhof, T.C., and Malenka, R.C. (2008). Understanding synapses: past, present, and future. Neuron 60 (3): 469-476.
Tai, H.C., Serrano-Pozo, A., Hashimoto, T., Frosch, M.P., Spires-Jones, T.L., and Hyman, B.T. (2012). The synaptic accumulation of hyperphosphorylated tau oligomers in Alzheimer disease is associated with dysfunction of the ubiquitin-proteasome system. Am J Pathol 181 (4): 1426-1435.
Tamagnini, F., Scullion, S., Brown, J.T., and Randall, A.D. (2015). Intrinsic excitability changes induced by acute treatment of hippocampal CA1 pyramidal neurons with exogenous amyloid beta peptide. Hippocampus 25 (7): 786-797.
Tamagnini, F., Walsh, D.A., Brown, J.T., Bondulich, M.K., Hanger, D.P., and Randall, A.D. (2017). Hippocampal neurophysiology is modified by a disease-associated C-terminal fragment of tau protein. Neurobiol Aging 60: 44-56.
Tracy, T.E., and Gan, L. (2018). Tau-mediated synaptic and neuronal dysfunction in neurodegenerative disease. Curr Opin Neurobiol 51: 134-138.
Tsay, D., Dudman, J.T., and Siegelbaum, S.A. (2007). HCN1 channels constrain synaptically evoked Ca2+ spikes in distal dendrites of CA1 pyramidal neurons. Neuron 56 (6): 1076-1089.
Turrigiano, G.G., and Nelson, S.B. (2004). Homeostatic plasticity in the developing nervous system. Nat Rev Neurosci 5 (2): 97-107.
Wahl-Schott, C., and Biel, M. (2009). HCN channels: structure, cellular regulation and physiological function. Cell Mol Life Sci 66 (3): 470-494.
Wang, H.S., Pan, Z., Shi, W., Brown, B.S., Wymore, R.S., Cohen, I.S., Dixon, J.E., and McKinnon, D. (1998). KCNQ2 and KCNQ3 potassium channel subunits: molecular correlates of the M-channel. Science 282 (5395): 1890-1893.
Wegmann, S., Bennett, R.E., Delorme, L., Robbins, A.B., Hu, M., McKenzie, D., Kirk, M.J., Schiantarelli, J., Tunio, N., Amaral, A.C.*, et al.* (2019). Experimental evidence for the age dependence of tau protein spread in the brain. Sci Adv 5 (6): eaaw6404.
Wishart, T.M., Parson, S.H., and Gillingwater, T.H. (2006). Synaptic vulnerability in neurodegenerative disease. J Neuropathol Exp Neurol 65 (8): 733-739.
Yuste, R., and Bonhoeffer, T. (2001). Morphological changes in dendritic spines associated with long-term synaptic plasticity. Annu Rev Neurosci 24: 1071-1089.
Zhou, L., McInnes, J., Wierda, K., Holt, M., Herrmann, A.G., Jackson, R.J., Wang, Y.C., Swerts, J., Beyens, J., Miskiewicz, K.*, et al.* (2017). Tau association with synaptic vesicles causes presynaptic dysfunction. Nat Commun. 8: 15295.

Figure 1

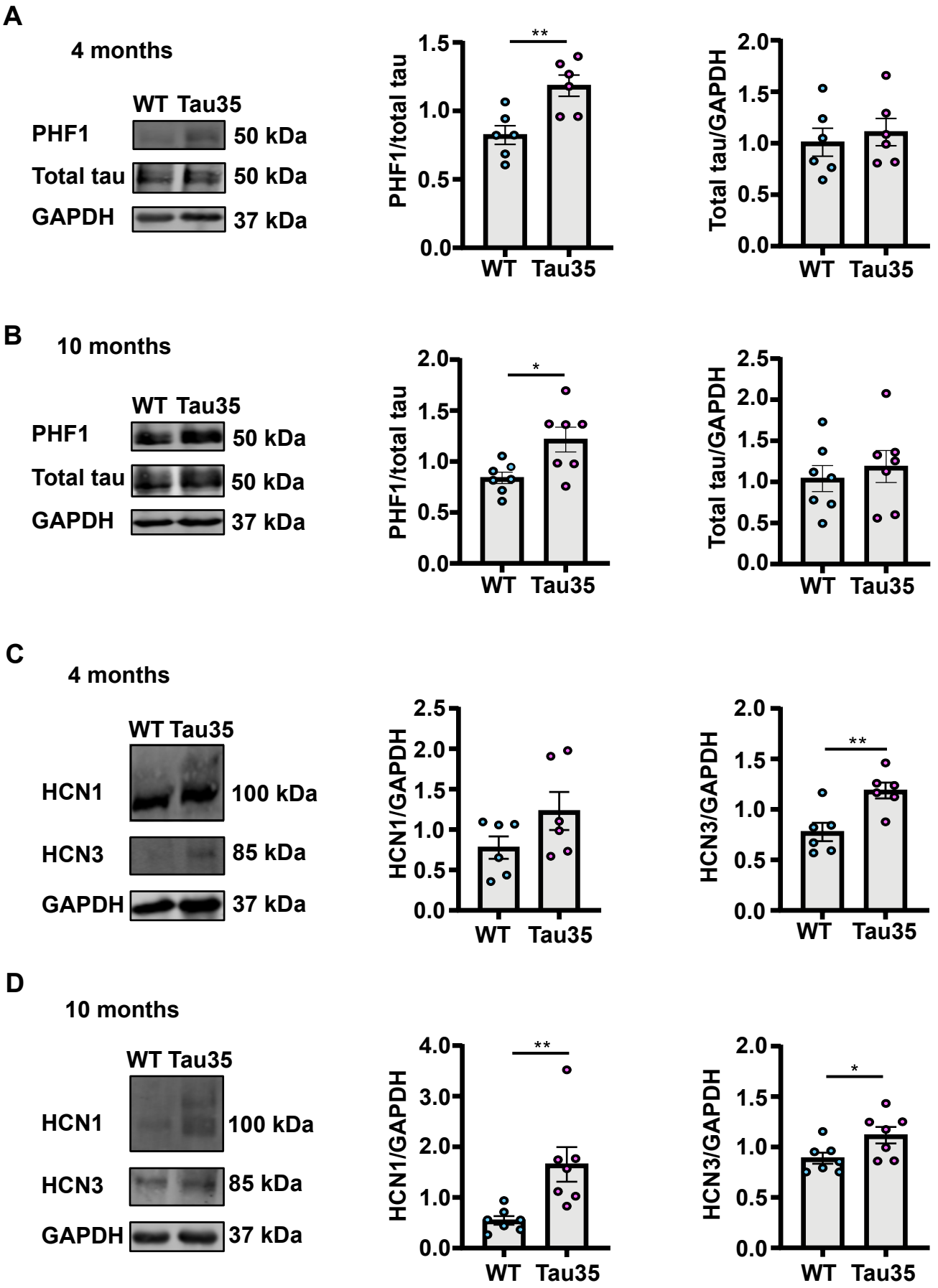
A
4 months
WT Tau35
PHF1
Total tau
GAPDH
50 kDa
50 kDa
37 kDa
PHF1/total tau
Total tau/GAPDH
WT Tau35
B
10 months
C
4 months
HCN1
HCN3
100 kDa
85 kDa
HCN1/GAPDH
HCN3/GAPDH
D
10 months

Figure 2

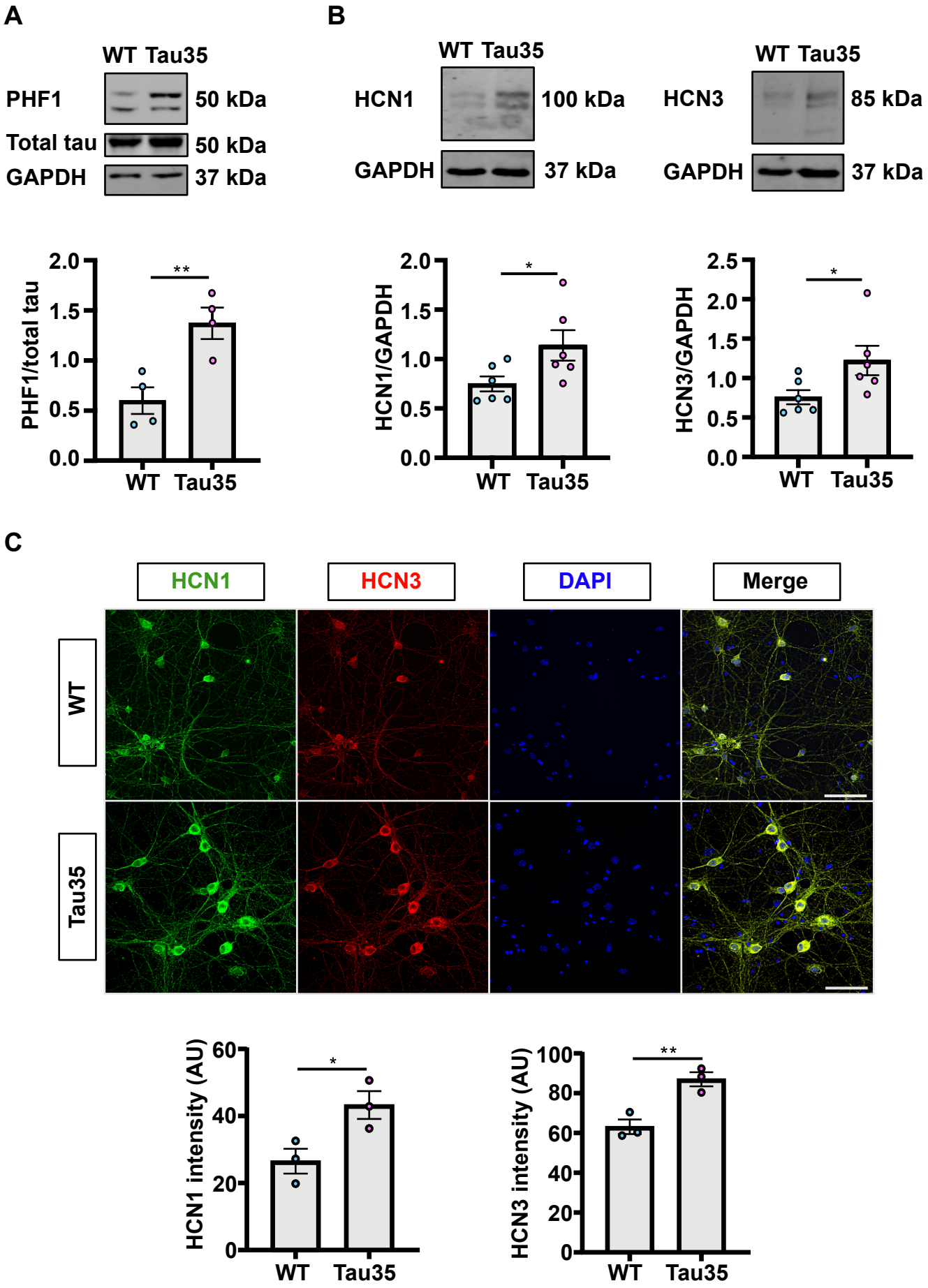
A
WT Tau35
PHF1
50 kDa
Total tau
50 kDa
GAPDH
37 kDa
PHF1/total tau
2.0
1.5
1.0
0.5
0.0
**
WT
Tau35
B
WT Tau35
HCN1
100 kDa
GAPDH
37 kDa
HCN1/GAPDH
*
WT Tau35
HCN3
85 kDa
GAPDH
37 kDa
HCN3/GAPDH
2.5
*
C
HCN1
HCN3
DAPI
Merge
WT
Tau35
HCN1 intensity (AU)
60
40
20
0
*
WT
Tau35
HCN3 intensity (AU)
100
80
60
40
20
0
**

Figure 3

A

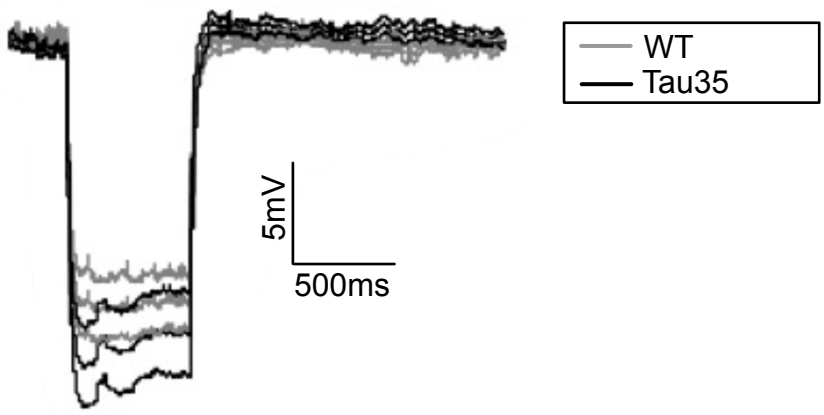
WT
Tau35
5mV
500ms

B

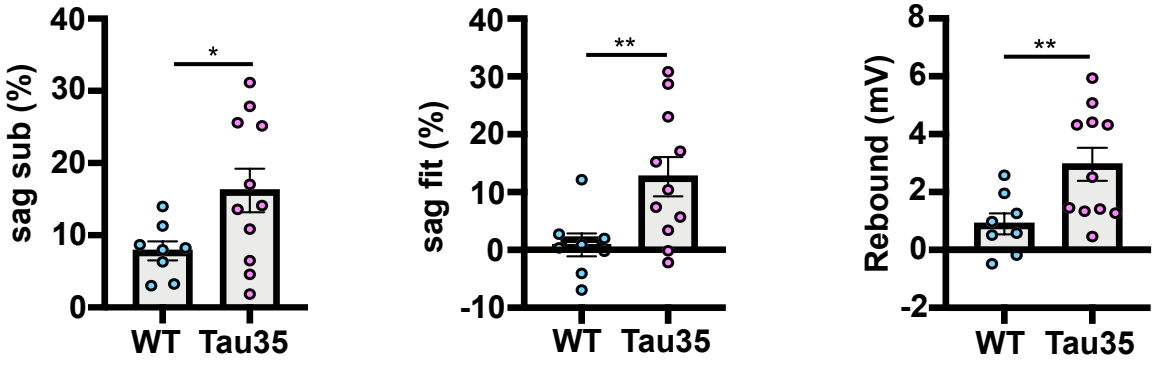
sag sub (%)
40
30
20
10
0
*
WT
Tau35
sag fit (%)
40
30
20
10
0
-10
**
WT
Tau35
Rebound (mV)
8
6
4
2
0
-2
**
WT
Tau35

Figure 4

A

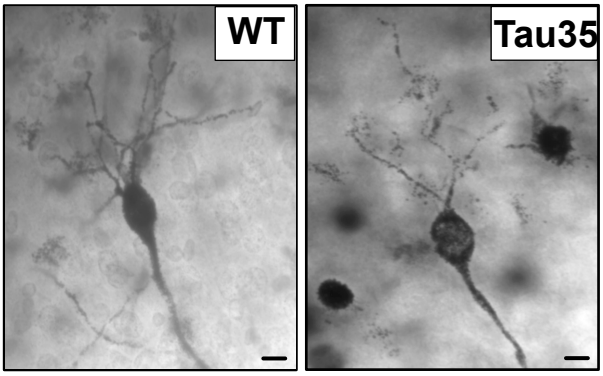
WT
Tau35

B

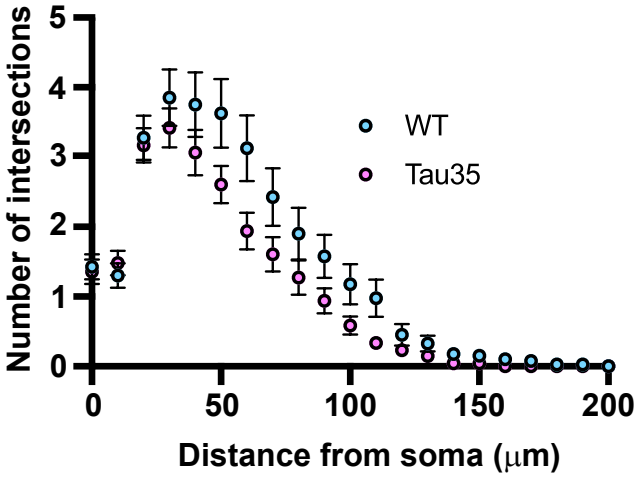
Number of intersections
0
1
2
3
4
5
0
50
100
150
200
Distance from soma (μm)
WT
Tau35

C

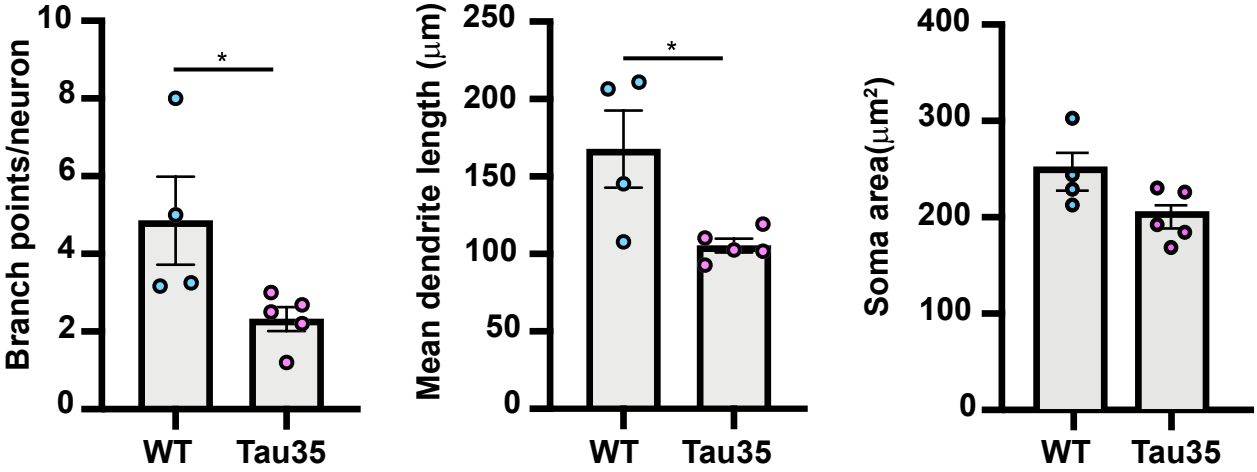
Branch points/neuron
0
2
4
6
8
10
*
WT
Tau35
Mean dendrite length (μm)
0
50
100
150
200
250
*
WT
Tau35
Soma area(μm²)
0
100
200
300
400
WT
Tau35

Figure 5

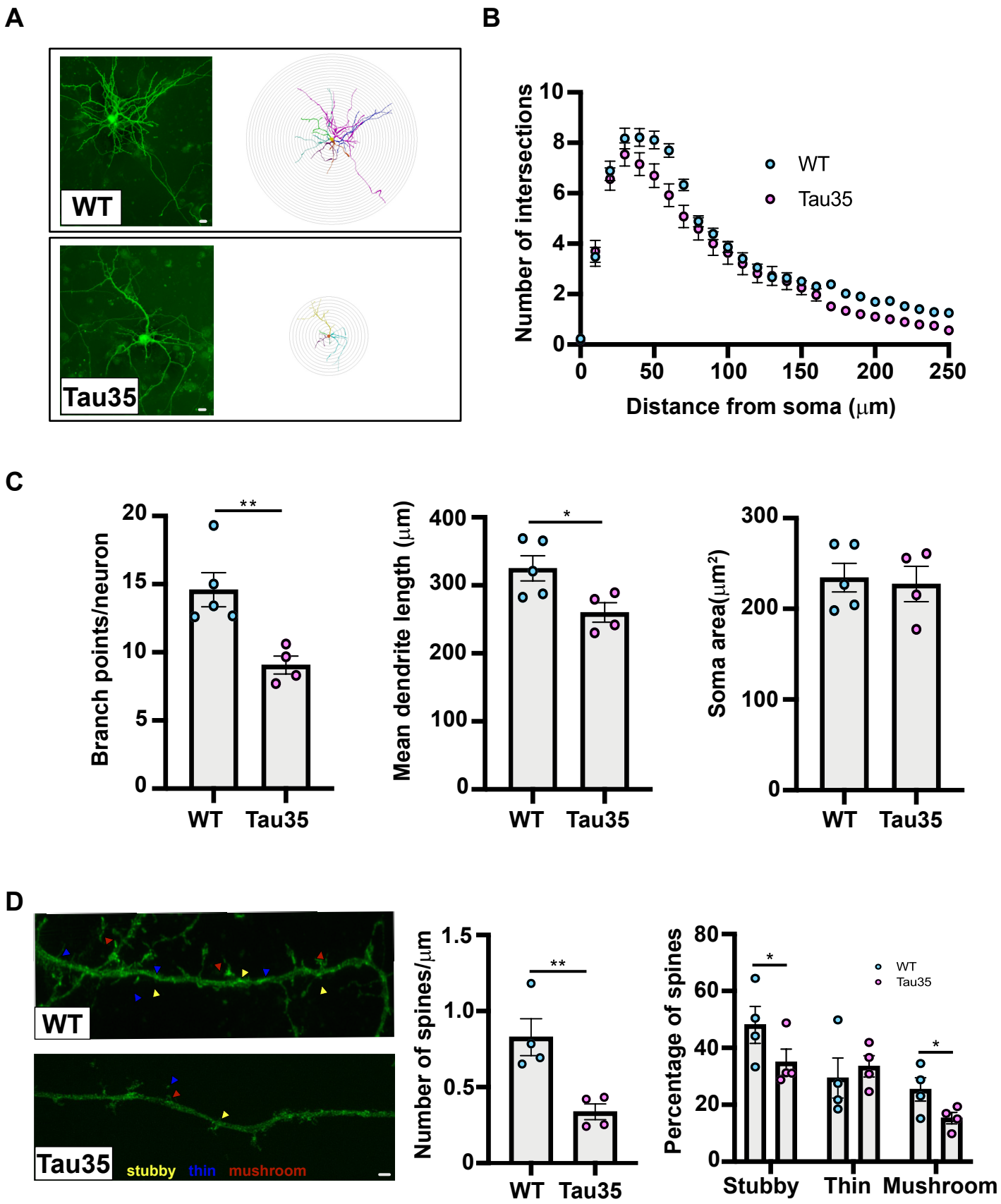
A
WT
Tau35
B
Number of intersections
Distance from soma (μm)
WT
Tau35
C
Branch points/neuron
Mean dendrite length (μm)
Soma area(μm²)
WT
Tau35
D
WT
Tau35
stubby
thin
mushroom
Number of spines/μm
Percentage of spines
Stubby
Thin
Mushroom

Figure 6

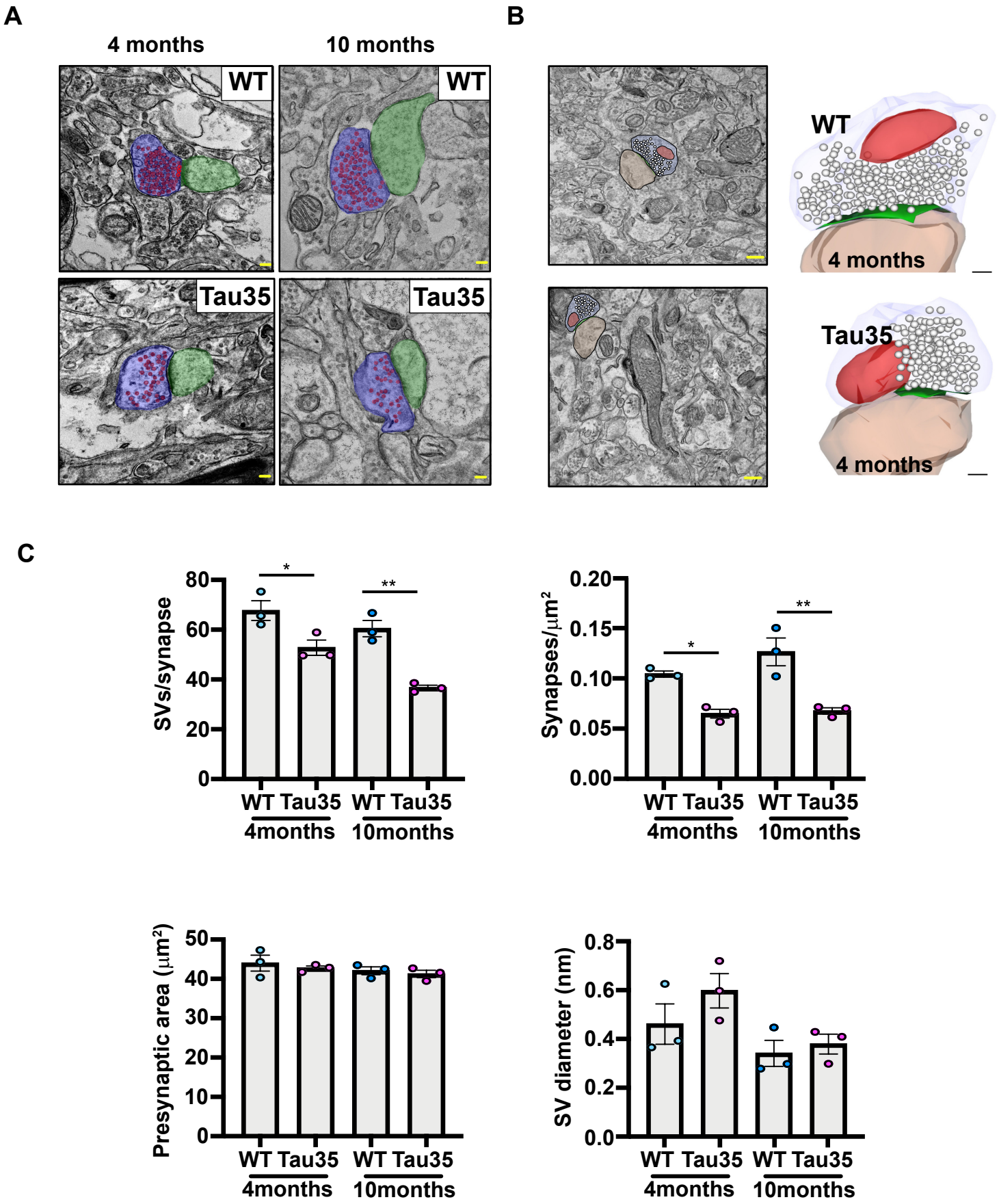
A
4 months
10 months
WT
WT
Tau35
Tau35
B
WT
4 months
Tau35
4 months
C
SVs/synapse
80
60
40
20
0
*
**
WT Tau35 WT Tau35
4months 10months
Synapses/μm²
0.20
0.15
0.10
0.05
0.00
*
**
WT Tau35 WT Tau35
4months 10months
Presynaptic area (μm²)
50
40
30
20
10
0
WT Tau35 WT Tau35
4months 10months
SV diameter (nm)
0.8
0.6
0.4
0.2
0.0
WT Tau35 WT Tau35
4months 10months

Figure 7

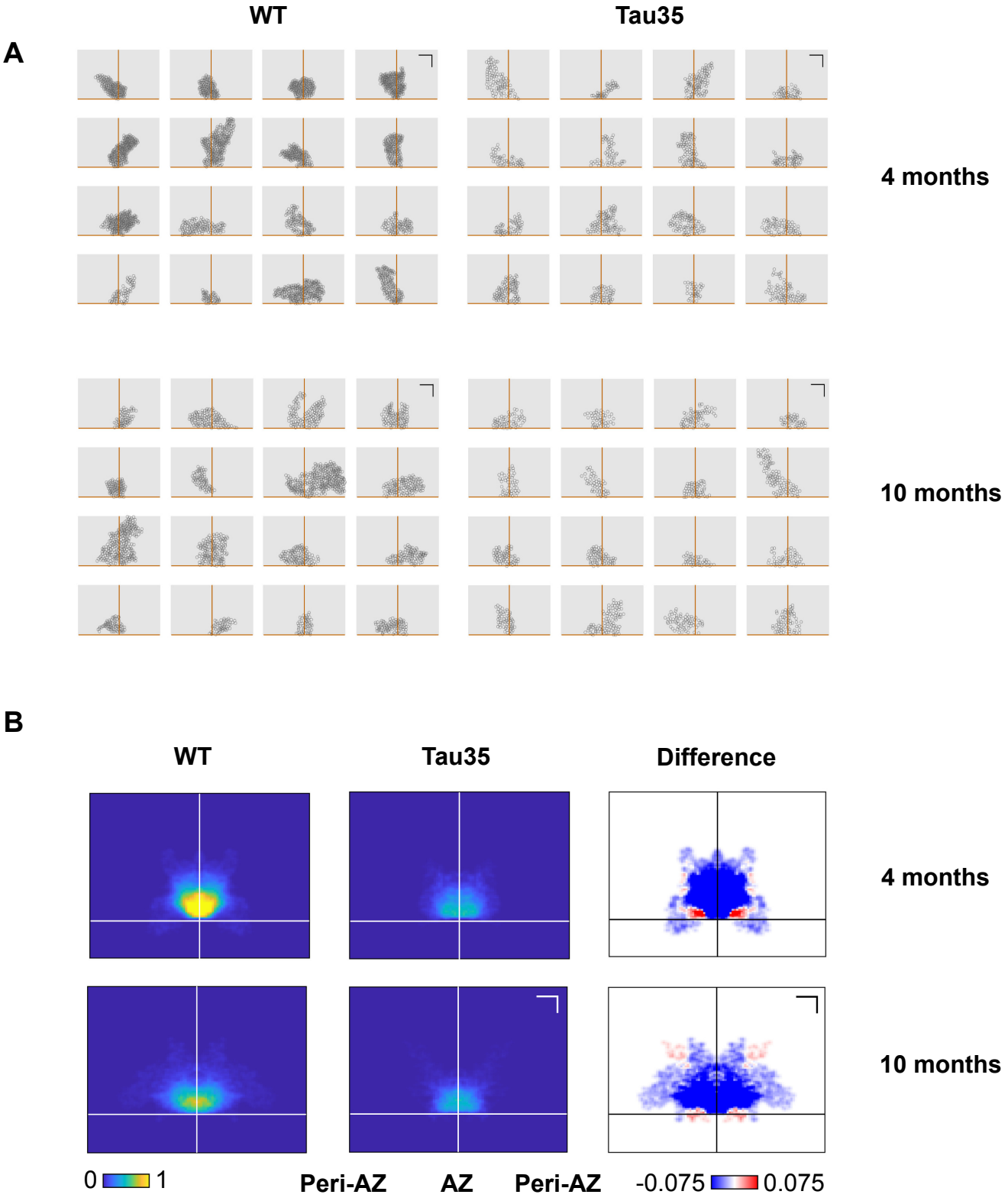
A
WT
Tau35
4 months
10 months
B
WT
Tau35
Difference
4 months
10 months
0
1
Peri-AZ
AZ
Peri-AZ
-0.075
0.075

Figure 8

A

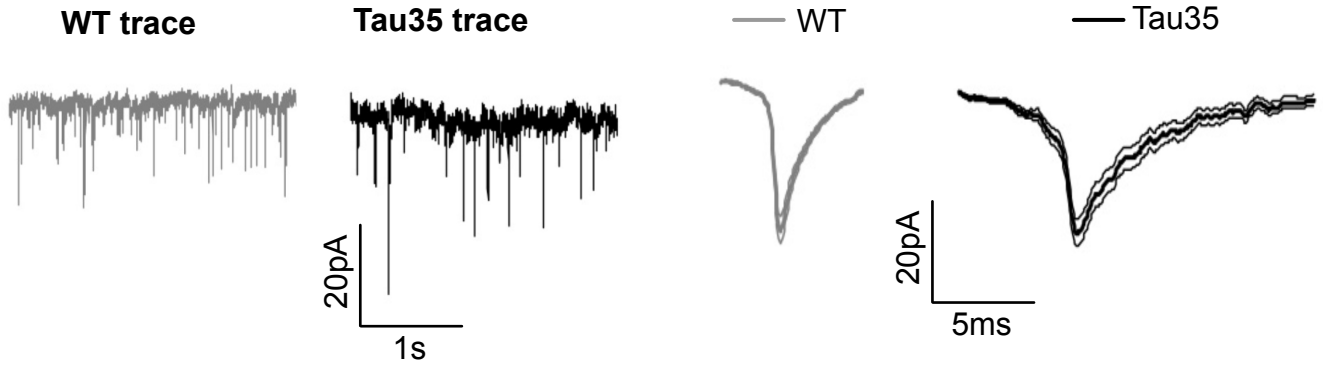
WT trace
Tau35 trace
WT
Tau35
20pA
1s
20pA
5ms

B

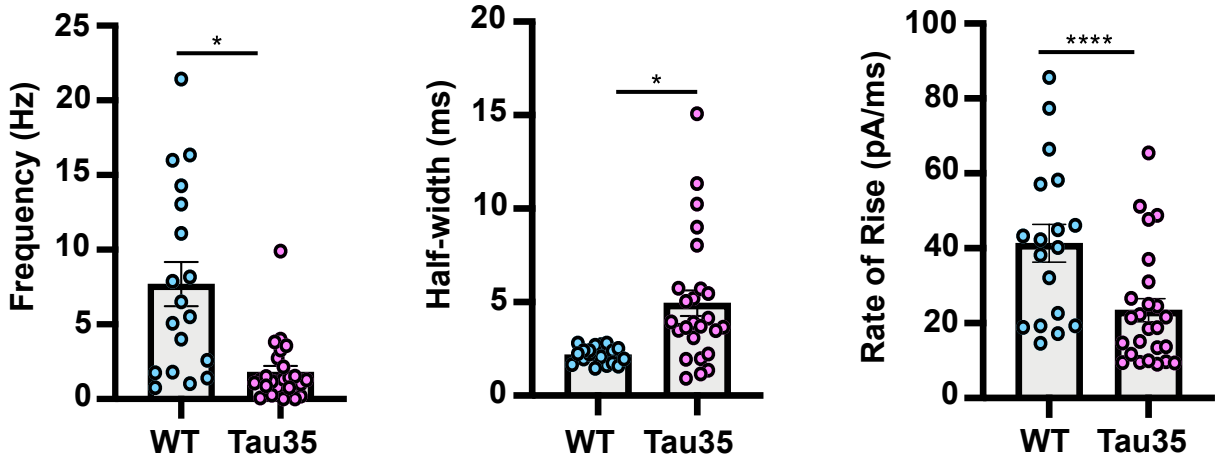
Frequency (Hz)
25
20
15
10
5
0
*
WT
Tau35
Half-width (ms)
20
15
10
5
0
*
WT
Tau35
Rate of Rise (pA/ms)
100
80
60
40
20
0
****
WT
Tau35